Tunable White-light Emission in Single Cation Templated Three-layered 2D Perovskites (CH3CH2NH3)4Pb3Br10-xClx

Lingling Mao, Yilei Wu, Constantinos C Stoumpos, Boubacar Traore, Claudine Katan, Jacky Even, Michael R Wasielewski, Mercouri G Kanatzidis

https://doi.org/10.1021/jacs.7b06143
J. Am. Chem. Soc. 2017, 139, 34, 11956–11963

Tunable White-light Emission in Single Cation Templated Three-layered 2D Perovskites $(CH_3CH_2NH_3)_4Pb_3Br_{10-x}Cl_x$

Lingling Mao[1], Yilei Wu[1], Constantinos C. Stoumpos[1], Boubacar Traore[3], Claudine Katan[3], Jacky Even[3], Michael R. Wasielewski[1,2] and Mercouri G. Kanatzidis*[1,2]

[1] Department of Chemistry, Northwestern University and [2]Argonne-Northwestern Solar Energy Research (ANSER) Center, Northwestern University, Evanston, Illinois 60208, United States

[3] Fonctions Optiques pour les Technologies de l'Information (FOTON), INSA de Rennes, CNRS, UMR 6082, 35708 Rennes, France.

ABSTRACT: Two-dimensional (2D) hybrid halide perovskites come as a family $(B)(A)_nPb_nX_{3n+1}$ (B, A= cations; X= halide). These perovskites are promising semiconductors for solar cells and optoelectronic applications. Among the fascinating properties of these materials is white-light emission, which has been mostly observed in single-layered 2D lead bromide or chloride systems (n = 1), where the broad emission comes from the transient photoexcited states generated by self-trapped excitons (STEs) from structural distortion. Here we report a multi-layered 2D perovskite (n = 3) exhibiting a tunable white-light emission. Ethylammonium (EA^+) can stabilize the 2D perovskite structure in $EA_4Pb_3Br_{10-x}Cl_x$ (x = 0, 2, 4, 6, 8, 9.5, 10) with EA^+ being both the A and B cations in this system. Because of the larger size of EA, these materials show a high distortion level in their inorganic structures with $EA_4Pb_3Cl_{10}$ having a much larger distortion than $EA_4Pb_3Br_{10}$, which results in broadband white-light emission in $EA_4Pb_3Cl_{10}$, while $EA_4Pb_3Br_{10}$ has narrow blue emission. The averaged lifetime of the series decreases gradually from the Cl end to the Br end, indicating the larger distortion also prolongs the lifetime (more STE states). The band gap of $EA_4Pb_3Br_{10-x}Cl_x$ ranges from 3.45 eV (x = 10) to 2.75 eV (x = 0), following the Vegard's law. First-principles Density Functional Theory calculations (DFT) show both $EA_4Pb_3Cl_{10}$ and $EA_4Pb_3Br_{10}$ are direct band gap semiconductors. The color rendering index (CRI) of the series improves from 66 ($EA_4Pb_3Cl_{10}$) to 83 ($EA_4Pb_3Br_{0.5}Cl_{9.5}$), displaying high tunability and versatility of the title compounds.

INTRODUCTION

Halide perovskite materials with hybrid organic-inorganic structures have captured the broad interest of the scientific community because their promises high performance photovoltaic (PV) and optoelectronic devices.[1-9] Among the leading materials, the $APbX_3$ perovskites are singled-out because they deliver the highest PV performance. However, the further utilization of the materials is hampered by the limited options in varying the A^+ cation which is limited to Cs, MA^+(MA^+ = $CH_3NH_3^+$) and FA^+(FA^+ = $HC(NH_2)_2^+$) which is due to stereochemical restrictions. Attempts to find alternative cations typically lead to unfavorable structures which do not have desirable semiconducting properties. An exception to this trend is seen in the case of 2D perovskites. Decreasing the dimensionality from three-dimensional (3D) to two-dimensional (2D), more versatile organic cations can be incorporated as templates to produce new structural types.[10] Compared to the single-layered 2D perovskites,[11-12] multi-layered 2D perovskites are less intensively investigated[13-15] but do promise superior properties in applications such as solar cells[16-19] and LEDs.[20-21] Multi-layered 2D systems also show better chemical stability than the 3D perovskite materials, as the longer organic cations are hydrophobic, making the devices moisture-stable.[16-18] As the "in-betweens" of the 3D compounds and the single-layered 2D compounds, multi-layered 2D perovskites of the formula $(B)(A)_nPb_nX_{3n+1}$ (B, A= cations; X= halide) can be tuned through multiple pathways: (1) layer thickness (i.e. value of n);[19, 22-23] (2) halide anion;[24] (3) metal cation; (4) organic spacer cation. All of these tunable components can be used to tailor the optical and electronic properties of the materials,[23, 25] to design materials for specific applications.

One of the emerging applications for perovskite materials comes in white light-emitting diodes (WLEDs) for solid state lighting. Single component white-light emitters have an easily controlled emission, better color rendering capability and reproducibility comparing to the multicomponent phosphors.[26-27] Unlike the doping strategy (rare earth ion into a host matrix), the energy transfer approach, white-light emitting nanocrystals[28-31] or other hybrid organic-inorganic white-light emitters,[27, 32] broad band emissions in perovskite materials are usually associated with structural distortions,[33-34] which gives rise to self-trapped excitons (STEs) due to strong electron-phonon coupling after photoexcitation.[35-36] Most of the reported white-light emitting perovskite materials up to date are single-layered 2D lead bromide or chloride perovskites, for instance $(C_6H_{13}N_3)PbBr_6$,[37] (N-MEDA) $PbBr_4$[38] (N-MEDA = N1-methylethane- 1,2-diammonium), $(EDBE)PbCl_4$, $(EDBE)PbBr_4$[39] (EDBE = 2,2'- (ethylenedioxy)bis(ethylammonium), $(C_6H_{11}NH_3)_2PbBr_4$[40], α-(DMEN)$PbBr_4$ (DMEN = 2-(dimethylamino)ethylamine)[33], $(C_6H_5C_2H_4NH_3)_2PbCl_4$[41] and (AEA)$PbBr_4$ (AEA = 3-(2-ammonioethyl)anilinium).[34]

In this work, we report the first example of multi-layered 2D perovskite with tunable white-light emission obtained from the use of ethylammonium ($CH_3CH_2NH_3^+$ = EA^+) cation. $EA_4Pb_3Cl_{10}$, $EA_4Pb_3Br_{10}$ and the $EA_4Pb_3Br_{10-x}Cl_x$ solid solu-

https://doi.org/10.1021/jacs.7b06143
J. Am. Chem. Soc. 2017, 139, 34, 11956–11963

tion are synthesized, and they represent a very rare example of a multilayer perovskite made of a single cation acting both as the B and A-cation in the structure of $(B)(A)_nPb_nX_{3n+1}$. The crystal structures of the $EA_4Pb_3Cl_{10}$ and $EA_4Pb_3Br_{10}$ perovskites are similar but the chloride analog is heavily distorted with respect to the bromide. The greater distortion is the result of the relatively large size of EA than the standard A-cations and smaller cage size of the chloride analog compared to the bromide. The PL emission reflects the structural distortion as $EA_4Pb_3Cl_{10}$ has a broadband white-light emission and $EA_4Pb_3Br_{10}$ has a narrow bandwidth of blue emission. To maximize the effect of STEs for broad emission, we further tune the compositions in the solid solutions, and find two of the intermediate compounds $EA_4Pb_3Br_{10-x}Cl_x$ (x = 8, 9.5) which have more optimized white-light emissions than $EA_4Pb_3Cl_{10}$. This provides a useful handle for controlling the photoluminescence (PL) properties in hybrid perovskite systems by utilizing the structure-PL relationship.

EXPERIMENTAL SECTION

Synthesis

Materials. PbO (99.9%), $PbCl_2$ (98%), $PbBr_2$ (98%), ethylamine hydrochloride (98%), hydrochloric acid (ACS reagent, 37%) and hydrobromic acid (ACS reagent, 48%) were purchased from Sigma-Aldrich and used as received.

Synthesis of $EA_4Pb_3Cl_{10}$. An amount of 1.338g (6 mmol) 99.9% PbO powder was dissolved in 20 ml of 37% hydrochloric acid by heating under stirring for 15 min at 180°C until solution turned colorless. 0.652g (8 mmol) of solid ethylamine hydrochloride was added directly to the above solution under heating and then kept under stirring until about 70% of the above solution was evaporated. If the solution is not concentrated enough, then $PbCl_2$ co-precipitates. Transparent rectangular plate-like crystals precipitated (Figure S2) during slow cooling to room temperature Yield 1.237g (53.3% based on total Pb content).

Synthesis of $EA_4Pb_3Br_{10}$. An amount of 1.338g (6 mmol) 99.9% PbO powder was dissolved in 10 ml of 48% hydrobromic acid by heating under stirring for 10 min at 180°C until solution turned colorless. 0.652g (8 mmol) of ethylamine hydrochloride was added directly to the above solution under heating. Yellow rectangular platelike crystals (Figure S2) precipitated during slow cooling. Yield 1.218g (37.9% based on total Pb content).

Synthesis of $EA_4Pb_3Br_{10-x}Cl_x$ (x = 9.5, 8, 6, 4, 2). Using solid-state grinding method, $EA_4Pb_3Br_{10-x}Cl_x$ (x = 9.5, 8, 6, 4, 2) were prepared with pre-synthesized EACl and EABr with $PbCl_2$ and $PbBr_2$. In a typical procedure for x = 8, 0.652g (8 mmol) of EACl with 1.112g (4 mmol) $PbCl_2$ and 0.734g (2 mmol) $PbBr_2$ was mixed and ground for 5 min. The homogenous mixture was annealed in the vacuum oven at 80°C for 2 hours. Rest of the series was synthesized using the same method with stoichiometric ratio of the cation source and anion source. Yield > 90%. The purity of the compounds was checked by Powder X-ray Diffraction (PXRD).

High-resolution Powder X-ray diffraction (PXRD) and Single Crystal X-ray Diffraction

High resolution synchrotron powder diffraction data were collected using beamline 11-BM at the Advanced Photon Source (APS), Argonne National Laboratory using an average wavelength of 0.517040 Å. Discrete 9 detectors covering an angular range from 0 to 4° 2θ are scanned over a 26° 2θ range, with data points collected every 0.001° 2θ and scan speed of 0.1°/s. Le Bail analysis was performed with the Jana2006 package.[37]

Full sphere data were collected after screening for a few frames using either a STOE IPDS 2 or IPDS 2T diffractometer with graphite-monochromatized Mo Kα radiation (λ = 0.71073 Å) (50 kV/40 mA) under N_2. The collected data was integrated and applied with numerical absorption corrections using the STOE X-AREA programs. Crystal structures were solved by charge flipping and refined by full-matrix least squares on F^2 with the Jana2006 package.[37]

Optical Absorption Spectroscopy

Optical diffuse reflectance measurements were performed using a Shimadzu UV-3600 UV-VIS-NIR spectrometer operating in the 200–1000 nm region using $BaSO_4$ as the reference of 100% reflectance. The band gap of the material was estimated by converting reflectance to absorption according to the Kubelka–Munk equation[42]: $\alpha/S = (1-R)^2(2R)^{-1}$, where R is the reflectance and α and S are the absorption and scattering coefficients, respectively.

Steady State and Time-resolved Photoluminescence.

Steady-state and time-resolved photoluminescence (TRPL) spectra were acquired using HORIBA Fluorolog-3 equipped with a 450-W xenon lamp and a TCSPC module (diode laser excitation at λ = 375 nm) and an integrating sphere (Horiba Quanta–φ) for absolute photoluminescence quantum yield determination. The spectra were corrected for the monochromator wavelength dependence and photomultiplier response functions provided by the manufacturer.

Electronic Structure Calculations.

https://doi.org/10.1021/jacs.7b06143
J. Am. Chem. Soc. 2017, 139, 34, 11956–11963

The calculations were performed within the Density Functional Theory (DFT)[43-44] as implemented in SIESTA package[45] with a basis set of finite-range of numerical atomic orbitals. We used the van der Waals density functional with C09 exchange (VDWC09)[46] to describe the exchange-correlation term. This functional has proven to provide superior description of experimental lattice constants similar to those obtained with optimized GGA based PBEsol functional in solids.[47] Norm-conserving Troullier-Martins pseudopotentials were used for each atomic species to account for the core electrons.[48] $1s^1$, $2s^22p^2$, $2s^22p^3$, $3s^23p^5$, $4s^24p^5$ and $5d^{10}6s^26p^2$ were used as valence electrons for H, C, N, Cl, Br and Pb respectively. Polarized Double-Zeta (DZP) basis set with an energy shift of 200 meV and a real space mesh grid energy cutoff of 200 Rydberg were used for the calculations. The Brillouin zone was sampled with 2×2×6 and 4×4×1 Monckhorst-Pack grids for the primitive cell and slab systems respectively. The electronic and dielectric properties were calculated with the experimental lattice parameters, and atomic coordinates were transformed to their primitive cells whenever applicable. Since the positions of H are not well resolved in these structures, they were optimized using VDW-C09 functional within the primitive cells while keeping the other atomic sites fixed. Spin-orbit coupling was taken into account in the calculation of the electronic band structures, although it was not considered in the high-frequency dielectric constant computations. For spin-orbit coupling, the revised PBE (revPBE) functional[49] was used. For the high-frequency dielectric constant profiles, slabs based on the respective systems were constructed, and an electric field of 0.01 eV/Å was applied along the [001] direction with the relaxation of the sole electron density as described elsewhere.[50-51]

RESULTS AND DISCUSSION

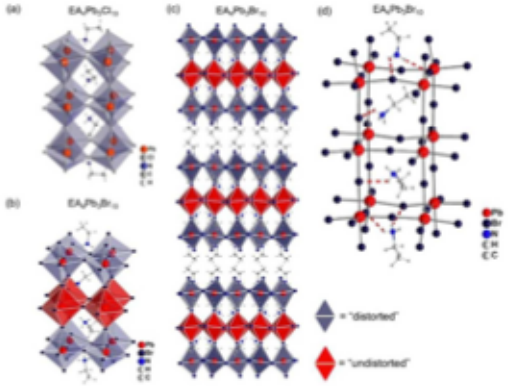

Figure 1. Structure fragment of the three-layered (a) $EA_4Pb_3Cl_{10}$ and (b) $EA_4Pb_3Br_{10}$. (c) Crystal structure of $EA_4Pb_3Br_{10}$, where the inner-layers compose of "undistorted" octahedra and outer-layers compose of "distorted" octahedra. (d) Hydrogen bonding network in $EA_4Pb_3Br_{10}$.

$EA_4Pb_3X_{10}$ (X = Br, Cl) belongs to the homologous series of layered perovskite phases $(B)(A)_nPb_nX_{3n+1}$ as defined above. In these structures B is the spacer cation that separates the inorganic layers, and A occupies the perovskite cages. In this case, EA acts as both the spacing A cation and the "perovskitizer" A' cation,[52] forming the three-layered (n = 3) structure. The $EA_4Pb_3Cl_{10}$ is the only known three-layered halide perovskite with a single kind of cation reported to date.[53] We have investigated this system with other halides (Br and I) and

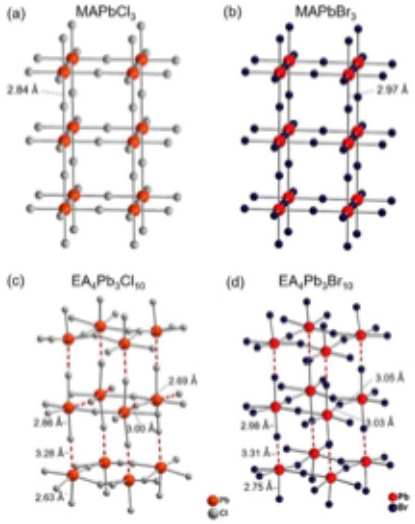

Figure 2. Pb-X (X = Cl or Br) bond lengths in (a) $MAPbCl_3$ (b) $MAPbBr_3$ (c) $EA_4Pb_3Cl_{10}$ and (d) $EA_4Pb_3Br_{10}$. The organic cations have been omitted for clarity.

found that Br^- can also stabilize the three-layered structure, while I^- cannot form the analogue with EA^+. Instead it forms a one-dimensional (1D) perovskite featuring chains of face-sharing octahedra.[54] In 3D $APbX_3$ perovskites, MA^+, FA+ and Cs+ are the only known cations that can fit in the framework. Because of the larger size of EA^+ cation the n = 3 perovskite layers are highly distorted to accommodate the extra $-CH_2-$ group as seen in Figure 1a. Compared to the chloride structure, the bromide analogue has undistorted "inner-layer" and

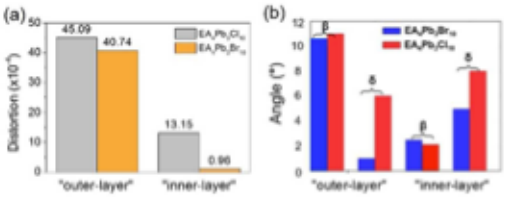

Figure 3. Comparison of the distortion level of "outer-layer" and "inner-layer" in $EA_4Pb_3Cl_{10}$ and $EA_4Pb_3Br_{10}$. From (a) Δd defined by equation (1) and (b) distortion angles defined in Figure 4.

https://doi.org/10.1021/jacs.7b06143
J. Am. Chem. Soc. 2017, 139, 34, 11956–11963

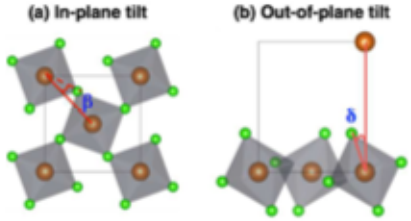

Figure 4. Definition of (a) the in-plane tilt angle β and (b) the out-of-plane tilt angle δ. β is the angle between the projected Pb1-X and Pb1-Pb2 to the plane perpendicular to the stacking axis. δ is the angle between Pb1'-X' and Pb1'-Pb2'. Note that Pb2' is the periodic image of Pb1'.

similarly very distorted "outer-layer" (Figure 1c). Since the ionic radius[55] of Br^- (1.95 Å) is larger than Cl^- (1.81 Å),[55] it is reasonable that it can better accommodate the EA^+ cation in the structure.

$EA_4Pb_3Cl_{10}$ crystallizes in the polar orthorhombic space group $A2_1ma$ (($=$ $Cmc2_1$), while $EA_4Pb_3Br_{10}$ crystallizes in the polar orthorhombic space group $C2cb$ ($=$ $Aba2$). Their detailed crystallographic parameters are given in Table S1. Both compounds consist of three layers of corner-connected $[PbX_6]^{4-}$ octahedra separated from one another with bilayers of EA^+ cations as "spacers" as seen in Figure 1c. Within the three-layers, EA^+ cations which act as "perovskitizers" filling the voids of the perovskite cavities (Figure 1d). The three-layer configuration requires a middle layer (the "inner-layer") and two symmetry related exterior layers (the "outer-layer"). From the lead halide framework, we can see that the distortion results in one short Pb-X bond and one long Pb-X bond from the [Pb-X-Pb] unit. In the 3D structure $MAPbCl_3$ and $MAPbBr_3$ (Figure 2a and 2b), all Pb-X bonds have the same length of 2.84 Å and 2.97 Å, respectively. For $EA_4Pb_3Cl_{10}$ however, short and long bond length combinations are seen in all directions. For example, in Figure 2c, the vertical Pb-Cl bonds of the bottom-left octahedron have length of 3.28 Å and 2.63 Å, which are respectively much longer and shorter than the Pb-Cl bond length (2.84 Å) in the 3D structure. The same "short-long" combinations have been observed for the "inner-layer" octahedra, as the horizontal Pb-Cl bond length of the middle-left octahedron in Figure 2c are 2.69 Å and 3.00 Å. For $EA_4Pb_3Br_{10}$, the distortion of the [Pb-X-Pb] unit only happens in the "outer-layer", as the bond lengths (3.05 Å and 3.03 Å) of the "inner-layer" are more equal and close to the 3D structure bond length (2.97 Å). To quantify the degree of the distortion, we define the octahedral distortion based on Pb-X bond lengths,[56-57]

$$\Delta d = \left(\frac{1}{6}\right)\sum\left[\frac{d_n - d}{d}\right]^2 \quad (1)$$

where d is the mean Pb-X bond distance and d_n are the six individual Pb-X bond distances (X = Br, Cl). In Figure 3, the "outer-layer" octahedra (layers next to the organic spacers, octahedra marked in purple in Figure 1c) of both $EA_4Pb_3Cl_{10}$ and $EA_4Pb_3Br_{10}$ have very high distortion level (Δd) of 45.09×10^{-4} and 40.74×10^{-4}, respectively. As for the "inner-

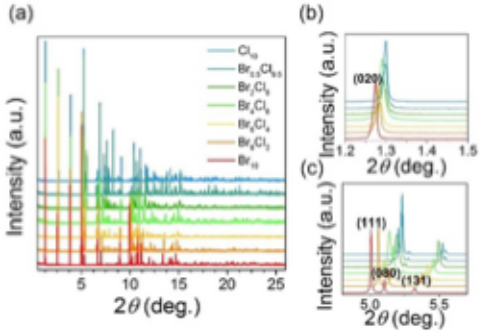

Figure 5. (a) High resolution PXRD of the $EA_4Pb_3Br_{10-x}Cl_x$ (x = 0, 2, 4, 6, 8, 9.5, 10) solid solution (synchrotron wavelength = 0.51704) (b) and (c) Peaks shift from higher angles to lower angles, suggesting increasing unit cell from x = 10 to x = 0.

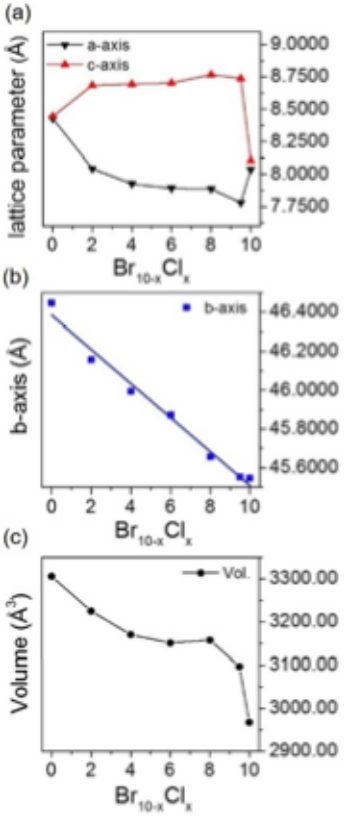

Figure 6. (a) (b) and (c) Unit cell parameters of the $EA_4Pb_3Br_{10-x}Cl_x$ (x = 0, 2, 4, 6, 8, 9.5, 10) solid solution.

https://doi.org/10.1021/jacs.7b06143
J. Am. Chem. Soc. 2017, 139, 34, 11956–11963

layer" octahedra, $EA_4Pb_3Cl_{10}$ still has a high distortion of 13.15×10^{-4} and $EA_4Pb_3Br_{10}$ has regular octahedra which are relatively undistorted ($\Delta d = 0.96\times10^{-4}$). Structural distortions are further manifested in the octahedral tilting defined by two tilt-angles β and δ as illustrated in Figure 4. These angles are linked to the evolution of the band gap with respect to the structural deformation of the perovskite. For all the layers except the β of the inner layers, β and δ (reported in Figure 3b and Table S2) are larger for $EA_4Pb_3Cl_{10}$ as compared to $EA_4Pb_3Br_{10}$, which is consistent with the more distorted Cl-based structure.

The advantage of a single cation as both the A cage cation and the spacer is that phase purity is much improved comparing to other 2D systems as it does not form other neighboring phases (e.g. n = 2, 4) because they are presumably less stable. This allows for the $EA_4Pb_3Br_{10-x}Cl_x$ (x = 2, 4, 6, 8, 9.5) solid solutions to be readily synthesized as pure phases using solid-state grinding at ~80°C. High-resolution PXRD data of the entire $EA_4Pb_3Br_{10-x}Cl_x$ series were collected using the beamline 11-BM at the APS (Figure 5). The lattice parameters of the solid solutions were extracted using Le Bail refinement method. Interestingly, the a and c axes are very similar to each other for both $EA_4Pb_3Br_{10}$ and $EA_4Pb_3Cl_{10}$. However, the intermediate compositions have a relatively large difference

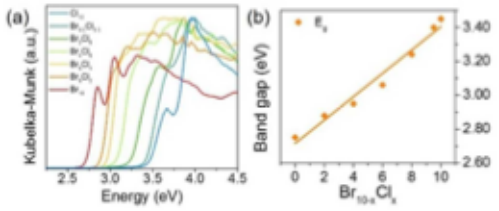

Figure 7. (a) Optical absorption spectra of $EA_4Pb_3Br_{10-x}Cl_x$ (x = 0, 2, 4, 6, 8, 9.5, 10). (b) Band gaps of the solid solution has a linear trend, which follows Vegard's law.

between a and c, for example $EA_4Pb_3Br_{0.5}Cl_{9.5}$ has the largest difference (a = 7.7807(2) (Å)) and c = 8.7393(2) (Å)), as seen in Figure 6a. The long axis, b, which runs perpendicular to the layers, decreases linearly from $EA_4Pb_3Br_{10}$ (b = 46.4483(3) Å) to $EA_4Pb_3Cl_{10}$ (b = 45.5452(6) Å). The unit cell volume also decreases from the Br end to the Cl end but not in a linear fashion as seen in Table 1 and Figure 6c. The anomaly in the evolution of the a and c axes for the intermediate compositions indicates that distortion occurs within the 2D inorganic layers which results in the amplification of the differences between the a and c axes. The difference between a and c axes gradually increases from x = 2 to x = 9.5, which suggest that the distortion increases when more Cl is incorporated in the structure.

The band gaps of the solid solution $EA_4Pb_3Br_{10-x}Cl_x$ (x = 0, 2, 4, 6, 8, 9.5, 10) exhibit a linear trend, following Vegard's law (Figure 7b). In this case the sharp absorption edge of the series is taken as the band gap, which ranges from 3.45 eV for $EA_4Pb_3Cl_{10}$ to 2.75 eV for $EA_4Pb_3Br_{10}$, and 3.40, 3.24, 3.06,

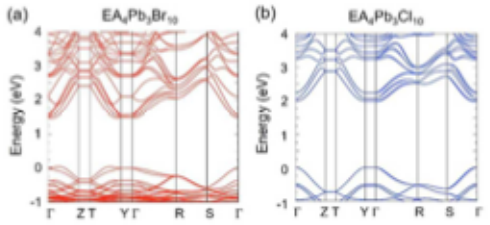

Figure 8. DFT calculations of electronic band structures for $EA_4Pb_3Br_{10}$ and $EA_4Pb_3Cl_{10}$, using the revPBE functional with SOC.

2.95, 2.88 eV respectively for the intermediates (Figure 6a). $EA_4Pb_3Br_{10}$ and $EA_4Pb_3Cl_{10}$ have clear excitonic features near the absorption edge and at higher energy (3.04 eV and 3.96 eV) as seen in Figure 7a, which are characteristic for 2D perovskites.[12, 23]

The DFT calculations show that $EA_4Pb_3Br_{10}$ and $EA_4Pb_3Cl_{10}$ are direct bandgap semiconductors, as expected for the halide perovskites in general, although they exhibit a slightly indirect character owing to the symmetry breaking (Rashba effect) (Figure 8). For $EA_4Pb_3Br_{10}$ the gap is slightly shifted away from Γ. A similar but smaller shift was also seen in $EA_4Pb_3Cl_{10}$ along the Γ [010] direction in reciprocal space. This shift away from a high-symmetry point of the Brillouin zone is a signature of Rashba effect in the polar structure of $EA_4Pb_3Br_{10}$ related to the giant spin-orbit coupling of the Pb atom. The calculated band gaps are 1.5 eV and 2.0 eV, respectively, when including SOC, showing a significant deviation from the experimental band gaps (2.75eV and 3.45eV, respectively. The calculated band gap of $EA_4Pb_3Cl_{10}$ is ~ 0.5 eV larger than that of $EA_4Pb_3Br_{10}$, which is comparable to the experimental band gap difference between the two compounds (~ 0.7 eV) but it also the difference between the corresponding 3D perovskites $MAPbCl_3$ and $MAPbBr_3$.[58]Unlike these 3D crystal structures, the electronic band structure in Figure 8 show flat dispersions between the Γ and Y k-points. This is indicative of little or vanishing electronic coupling along this direction, which coincides with the stacking axis.

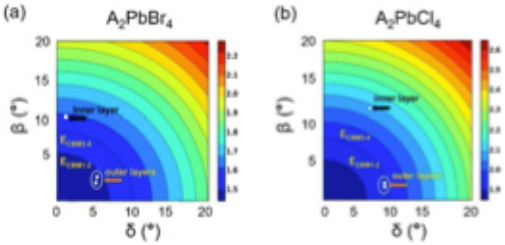

Figure 9. 2D color map of the electronic band gap variation including spin-orbit coupling with respect to octahedral distortions defined in Figure 4 for model systems A_2PbBr_4 and A_2PbCl_4 (A = Cs). Distortion angles of the inner and outer octahedral layers for $EA_4Pb_3Br_{10}$ and $EA_4Pb_3Cl_{10}$ are pointed to by the arrows in A_2PbBr_4 and A_2PbCl_4 respectively. ECBM1-2 and ECBM3-4 indicate the contour levels corresponding to their values from the band structure of Figure 7.

https://doi.org/10.1021/jacs.7b06143
J. Am. Chem. Soc. 2017, 139, 34, 11956–11963

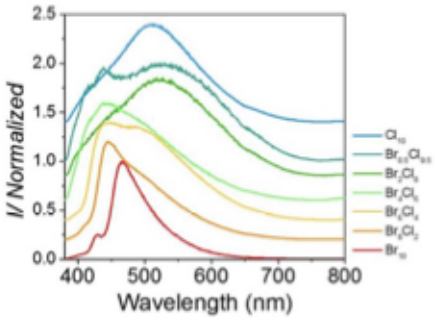

Figure 10. Steady-state PL of $EA_4Pb_3Br_{10-x}Cl_x$ (x = 0, 2, 4, 6, 8, 9.5, 10) (λ_{exc} = 315 nm).

The nature of the valence band maximum (VBM) and conduction band minimum (CBM) states can be captured by computing corresponding wave functions Ψ (without SOC) or local density of states (LDOS, with SOC). Ψ at Γ (Figure S8 and Figure S9) for both compounds show an anti-bonding hybridization between Pb 6s and p orbitals of the halides at the VBM while the CBM is mainly of Pb 6p type.[59] Consistent with the wave functions, the LDOS of VBM mostly localize on the inner octahedral layer, while those of CBM localize on the outer layers (Figure S10). For $EA_4Pb_3Cl_{10}$, both Ψ and LDOS are also partly present on the inner layer, indicative of a weaker charge separation across the layers. Hence, because of the spatial separation between VBM and CBM wave functions, we expect a more stable $EA_4Pb_3Cl_{10}$. The high-frequency dielectric constants are deduced from the computed dielectric profiles (Figure S12) and amount to 3.9 and 3.5 for $EA_4Pb_3Br_{10}$ and $EA_4Pb_3Cl_{10}$, respectively. Compared to the 3D compounds $MAPbBr_3$ (ε_∞ = 5.2) and $MAPbCl_3$ (ε_∞ = 4.2),[60] the EA system shows smaller dielectric confinement.

Previous studies have demonstrated that structural deformation has a significant effect on the band gap of hybrid perovskites which is directly linked to their optical properties.[58, 61-63] To rationalize the interplay between octahedral distortions and band gap variation in $EA_4Pb_3Br_{10}$ and $EA_4Pb_3Cl_{10}$, we built model systems of A_2PbBr_4 and A_2PbCl_4 (A = Cs), similar to the A_2PbI_4 model (n = 1) proposed earlier.[25] Figure 9 shows the 2D color map of the electronic band gap variation with respect to the β and δ angles defined in Figure 4. The band gap increases with increasing structural deformation in agreement with previous works.[25, 64] Interestingly, for both $EA_4Pb_3Br_{10}$ and $EA_4Pb_3Cl_{10}$, the band gap predicted when considering the (β, δ) angles of the "outer-layers" fit nicely to the calculated band gaps on the real crystal structures shown Figure 8. This is consistent with the fact that band edge states (VBM and CBM) in hybrid halide perovskites are mainly determined by the inorganic framework, and are produced by the hybridization of Pb and X atomic orbitals. Furthermore, the band gap variation obtained using (β, δ) of the inner and outer layers of $EA_4Pb_3Br_{10}$ and $EA_4Pb_3Cl_{10}$ reveal a sizeable difference. The variation in $EA_4Pb_3Br_{10}$ is half that of the $EA_4Pb_3Cl_{10}$ with two and three contour levels difference, respectively. This indicates that the electronic band gap fluctuations in $EA_4Pb_3Cl_{10}$ which derive from the structural distortion are larger than in $EA_4Pb_3Br_{10}$. As such, the spread in octahedral distortions is predicted to strongly broaden the emission spectra of $EA_4Pb_3Cl_{10}$.

Such a broadening is indeed observed by PL measurements. In fact, a broadband white-light emission is observed for $EA_4Pb_3Cl_{10}$ (peak centered at 500 nm, FWHM = 151 nm). The PL of the whole $EA_4Pb_3Br_{10-x}Cl_x$ series shows a different trend than that obtained for absorption as seen in Figure 10. It starts with. The intermediates x = 9.5 and 8 have even broader emission (FWHM = 228 nm and 187 nm), which could be due to

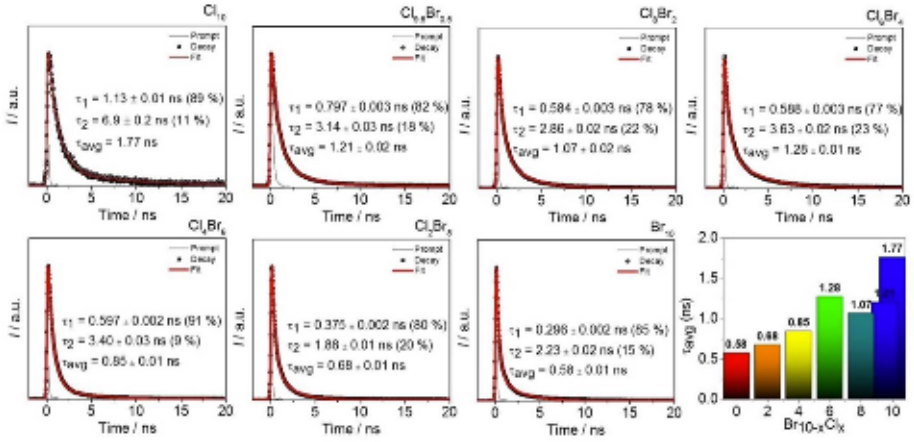

Figure 11. Time-resolved PL decays and fitting of $EA_4Pb_3Br_{10-x}Cl_x$ (x = 0, 2, 4, 6, 8, 9.5, 10). The averaged PL decay lifetime shows a decreasing trend from x = 10 to x = 0 (λ_{exc} = 375 nm).

https://doi.org/10.1021/jacs.7b06143
J. Am. Chem. Soc. 2017, 139, 34, 11956–11963

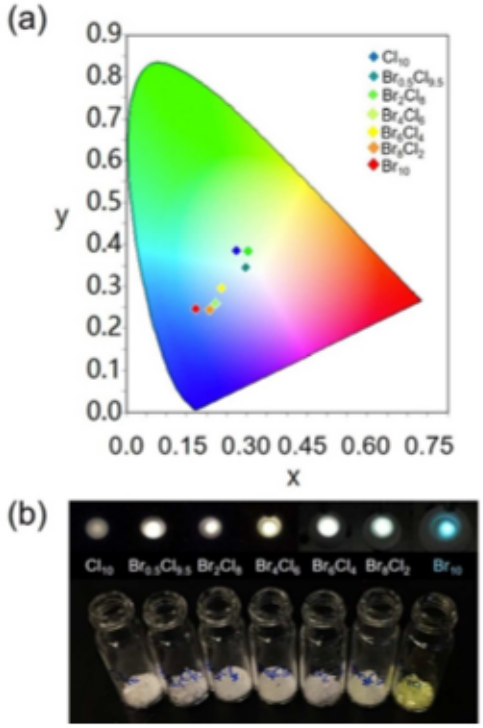

Figure 12. (a) CIE color coordinates of $EA_4Pb_3Br_{10-x}Cl_x$ (x = 0, 2, 4, 6, 8, 9.5, 10) in 1931 color space chromaticity diagram. Detailed values are given in Table 1. (b) White-light emissions from $EA_4Pb_3Br_{10-x}Cl_x$ (x = 2, 4, 6, 8, 9.5, 10) and blue-light emission from $EA_4Pb_3Br_{10}$ (excited at 315nm). Corresponding powered polycrystalline samples are shown on the bottom.

the large difference in a and c axis caused by distortion along the layers as discussed in the previous paragraph. The bandwidth of the emission decreases from x = 9.5, becoming narrower all the way to the Br end member, which has an emission peak at 465 nm (2.67 eV). The bandwidth of the PL emission is anticipated since $EA_4Pb_3Cl_{10}$ has a much more distorted structure than $EA_4Pb_3Br_{10}$ and therefore it is expected to have more STEs states and broader emission.[33] In Figure 11, time-resolved PL reveals that the average lifetime of the series decreases from being the longest in the Cl end member (τ_{avg} = 1.77 ns) to shortest in the Br end member (τ_{avg} = 0.58 ns), further confirming the correlation between structural distortion and PL (bandwidth and lifetime). Both the bond length variation in the octahedron and the angular (β, δ) distortion within the inorganic framework contributed to the overall broadening in the PL emission.

The light emission properties of the $EA_4Pb_3Br_{10-x}Cl_x$ (x = 0, 2, 4, 6, 8, 9.5, 10) are highly tunable, from cold white-light to relatively warm white-light as seen in Figure 12. The Commission International de l'Eclairage (CIE) color coordinates of these compounds shift from close to the center to the blue region in the 1931 color space chromaticity diagram in Figure 12a. Compared to $EA_4Pb_3Cl_{10}$ (0.27, 0.39), $EA_4Pb_3Br_{0.5}Cl_{9.5}$ and $EA_4Pb_3Br_2Cl_8$ have CIE coordinates closer to the white point (0.33, 0.33), which are (0.30, 0.35) and (0.30, 0.38), respectively. The Color Rendering Indexes (CRI) are also significantly improved from 66 (Cl_{10}) to 83 ($Br_{0.5}Cl_{9.5}$) as seen in Table 1, giving much better quality of color rendering of the emission. Compared to our previous studied compound α-(DMEN)$PbBr_4$ (CRI = 7 3, CIE coordinates (0.28, 0.36)), the current system shows improved CRI with two compositions (x = 8, 9.5). The Correlated Color Temperatures (CCT) of the series are all above 6000K, suggesting these materials are emitting "cold" white-light.

CONCLUSIONS

The new series of 2D perovskites $EA_4Pb_3X_{10}$ (X = Cl, Br), is unique because it features a single A-cation acting both as a spacer and a "perovskitizer" cation. The large size of the EA

Table 1. Lattice parameters (based on space group *C2cb/A2₁ma*), Commission International de l'Eclairage (CIE) color coordinates (x, y), Correlated Color Temperature (CCT), Color Rendering Index (CRI) and full-width at half-maximum (FWHM) of $EA_4Pb_3Br_{10-x}Cl_x$ (x = 0, 2, 4, 6, 8, 9.5, 10).

Compound	*a (Å)*	*b (Å)*	*c (Å)*	*Volume*	*x*	*y*	*CCT (K)*	*CRI*	*FWHM (nm)*
Cl_{10}	8.0375(1)	45.5452(6)	8.1064(1)	2967.52(0)	0.27	0.39	7720	66	151
$Br_{0.5}Cl_{9.5}$	7.7807(2)	45.5530(12)	8.7393(2)	3097.51(0)	0.30	0.35	7132	83	228
Br_2Cl_8	7.8876(5)	45.6569(25)	8.7684(4)	3157.70(5)	0.30	0.38	6564	75	187
Br_4Cl_6	7.8921(4)	45.8723(18)	8.7038(4)	3151.05(3)	0.22	0.26	52126	N/A	147
Br_6Cl_4	7.9267(2)	45.9958(15)	8.6952(3)	3170.25(0)	0.24	0.30	15405	75	153
Br_8Cl_2	8.0443(1)	46.1571(5)	8.6860(2)	3225.12(0)	0.21	0.24	950000	N/A	98
Br_{10}	8.4297(1)	46.4483(3)	8.4432(1)	3305.90(0)	0.17	0.24	N/A	N/A	61

cation (2.74 Å) relative to MA (2.17 Å)[65] introduces a severe structural distortion to the perovskite layers which becomes more prominent for the smaller Cl anions. The structural distortions lead to a white-light emission which can be understood in terms of an amplified STEs process. The highly distorted Pb-X framework helps to generate more transient photoexcited STEs states resulting from strong electron-phonon coupling, while also prolongs the process which is demonstrated in longer PL lifetime observed. The different distortion levels in $EA_4Pb_3Cl_{10}$ (large distortion) vs $EA_4Pb_3Br_{10}$ (small distortion) result in different PL emission bandwidth, where $EA_4Pb_3Cl_{10}$ has a broadband white-light emission while $EA_4Pb_3Br_{10}$ has a narrow blue emission. The emission properties can be conveniently tuned in the $EA_4Pb_3Br_{10-x}Cl_x$ (x = 0, 2, 4, 6, 8, 9.5, 10) solid solution. The band gap of the series follows the Vegard's law, increasing linearly from x = 0 to x = 10. Time-resolved PL measurements also show a gradual increase of average lifetimes from the Br end to Cl end, showing the dependency of emissive STEs states on the structure composition. From DFT simulation, it is shown that the optoelectronic properties of $EA_4Pb_3Cl_{10}$ are more sensitive to the structural disorder leading to a dispersion of the electronic band gap and to exciton localization, which correlates well with longer average radiative lifetime. $EA_4Pb_3Br_{0.5}Cl_{9.5}$ has the highest CRI (CRI = 83) in the series, providing better color rendering than the pure Cl compound $EA_4Pb_3Cl_{10}$ (CRI = 66). This series of hybrid materials are promising candidates for solid state lighting as they demonstrate high tunability and have clear structure-PL relationships.

ASSOCIATED CONTENT

Supporting Information

Additional PL data and crystallographic details (PDF and CIF). This material is available free of charge via the Internet at http://pubs.acs.org.

AUTHOR INFORMATION

Corresponding Author

*Email: m-kanatzidis@northwestern.edu

Notes

The authors declare no competing financial interests.

ACKNOWLEDGMENT

This work was supported by the Department of Energy, Office of Science, Basic Energy Sciences, under Grant SC0012541. Y.W. thanks the Fulbright Scholars Program for a Graduate Research Fellowship and gratefully acknowledges support of a Ryan Fellowship from the NU International Institute for Nanotechnology (IIN). Use of the Advanced Photon Source at Argonne National Laboratory was supported by the U. S. Department of Energy, Office of Science, Office of Basic Energy Sciences, under Contract No. DE-AC02-06CH11357.

REFERENCES

1. Kojima, A.; Teshima, K.; Shirai, Y.; Miyasaka, T., *J. Am. Chem. Soc.* **2009,** *131*, 6050-6051.
2. Stoumpos, C. C.; Kanatzidis, M. G., *Acc. Chem. Res.* **2015,** *48*, 2791-2802.
3. Stranks, S. D.; Snaith, H. J., *Nat. Nanotechnol.* **2015,** *10*, 391-402.
4. Stoumpos, C. C.; Kanatzidis, M. G., *Adv. Mater.* **2016,** *28*, 5778-5793.
5. Park, N.-G.; Grätzel, M.; Miyasaka, T.; Zhu, K.; Emery, K., *Nat. Energy* **2016,** *1*, 16152.
6. Correa-Baena, J.-P.; Abate, A.; Saliba, M.; Tress, W.; Jacobsson, T. J.; Grätzel, M.; Hagfeldt, A., *Energy Environ Sci.* **2017,** *10*, 710-727.
7. Xiao, Z.; Meng, W.; Wang, J.; Mitzi, D. B.; Yan, Y., *Mater. Horiz.* **2017,** *4*, 206-216.
8. Im, J.-H.; Lee, C.-R.; Lee, J.-W.; Park, S.-W.; Park, N.-G., *Nanoscale* **2011,** *3*, 4088-4093.
9. Kim, H.-S.; Lee, C.-R.; Im, J.-H.; Lee, K.-B.; Moehl, T.; Marchioro, A.; Moon, S.-J.; Humphry-Baker, R.; Yum, J.-H.; Moser, J. E., *Sci. Rep.* **2012,** *2*, 591.
10. Saparov, B.; Mitzi, D. B., *Chem. Rev.* **2016,** *116*, 4558-4596.
11. Cheng, Z.; Lin, J., *CrystEngComm* **2010,** *12*, 2646-2662.
12. Mao, L.; Tsai, H.; Nie, W.; Ma, L.; Im, J.; Stoumpos, C. C.; Malliakas, C. D.; Hao, F.; Wasielewski, M. R.; Mohite, A. D.; Kanatzidis, M. G., *Chem. Mater.* **2016,** *28*, 7781-7792.
13. Mitzi, D.; Feild, C.; Harrison, W.; Guloy, A., *Nature* **1994,** *369*, 467-469.
14. Mitzi, D.; Wang, S.; Feild, C.; Chess, C.; Guloy, A., *Science* **1995,** *267*, 1473.
15. Kagan, C. R.; Mitzi, D. B.; Dimitrakopoulos, C. D., *Science* **1999,** *286*, 945-947.
16. Smith, I. C.; Hoke, E. T.; Solis - Ibarra, D.; McGehee, M. D.; Karunadasa, H. I., *Angew. Chem. Int. Ed.* **2014,** *126*, 11414-11417.
17. Cao, D. H.; Stoumpos, C. C.; Farha, O. K.; Hupp, J. T.; Kanatzidis, M. G., *J. Am. Chem. Soc* **2015,** *137*, 7843-7850.
18. Tsai, H.; Nie, W.; Blancon, J.-C.; Stoumpos, C. C.; Asadpour, R.; Harutyunyan, B.; Neukirch, A. J.; Verduzco, R.; Crochet, J. J.; Tretiak, S.; Pedesseau, L.; Even, J.; Alam, M. A.; Gupta, G.; Lou, J.; Ajayan, P. M.; Bedzyk, M. J.; Kanatzidis, M. G.; Mohite, A. D., *Nature* **2016,** *536*, 312-316.
19. Stoumpos, C. C.; Soe, C. M. M.; Tsai, H.; Nie, W.; Blancon, J.-C.; Cao, D. H.; Liu, F.; Traoré, B.; Katan, C.; Even, J., *Chem* **2017,** *2*, 427-440.

20. Yuan, M.; Quan, L. N.; Comin, R.; Walters, G.; Sabatini, R.; Voznyy, O.; Hoogland, S.; Zhao, Y.; Beauregard, E. M.; Kanjanaboos, P.; Lu, Z.; Kim, D. H.; Sargent, E. H., *Nat. Nanotechnol.* **2016,** *11*, 872–877.
21. Congreve, D. N.; Weidman, M. C.; Seitz, M.; Paritmongkol, W.; Dahod, N. S.; Tisdale, W. A., *ACS Photonics* **2017,** *4*, 476-481.
22. Hassan, Y.; Song, Y.; Pensack, R. D.; Abdelrahman, A. I.; Kobayashi, Y.; Winnik, M. A.; Scholes, G. D., *Adv. Mater.* **2016,** *28*, 566-573.
23. Stoumpos, C. C.; Cao, D. H.; Clark, D. J.; Young, J.; Rondinelli, J. M.; Jang, J. I.; Hupp, J. T.; Kanatzidis, M. G., *Chem. Mater.* **2016,** *28*, 2852-2867.
24. Aharon, S.; Etgar, L., *Nano lett.* **2016,** *16*, 3230-3235.
25. Pedesseau, L.; Sapori, D.; Traore, B.; Robles, R.; Fang, H.-H.; Loi, M. A.; Tsai, H.; Nie, W.; Blancon, J.-C.; Neukirch, A., *ACS nano* **2016,** *10*, 9776-9786.
26. Shang, M.; Li, C.; Lin, J., *Chem. Soc. Rev.* **2014,** *43*, 1372-1386.
27. Wang, M.-S.; Guo, G.-C., *Chem. Commun.* **2016,** *52*, 13194-13204.
28. Zhao, Y. S.; Fu, H.; Hu, F.; Peng, A.; Yang, W.; Yao, J., *Adv. Mater.* **2008,** *20*, 79-83.
29. Bowers, M. J.; McBride, J. R.; Rosenthal, S. J., *J. Am. Chem. Soc.* **2005,** *127*, 15378-15379.
30. Sapra, S.; Mayilo, S.; Klar, T. A.; Rogach, A. L.; Feldmann, J., *Adv. Mater.* **2007,** *19*, 569-572.
31. Yang, G.; Xu, G.; Chen, B.; Zou, S.; Liu, R.; Zhong, H.; Zou, B., *Chem.Mater.* **2013,** *25*, 3260-3266.
32. Carlos, L.; Sá Ferreira, R.; Pereira, R.; Assunção, M.; de Zea Bermudez, V., *J. Phys. Chem. B* **2004,** *108*, 14924-14932.
33. Mao, L.; Wu, Y.; Stoumpos, C. C.; Wasielewski, M. R.; Kanatzidis, M. G., *J. Am. Chem. Soc.* **2017,** *139*, 5210-5215.
34. Smith, M. D.; Jaffe, A.; Dohner, E. R.; Lindenberg, A.; Karunadasa, H. I., *Chem. Sci.* **2017,** *8*, 4497-4504.
35. Hu, T.; Smith, M. D.; Dohner, E. R.; Sher, M.-J.; Wu, X.; Trinh, M. T.; Fisher, A.; Corbett, J.; Zhu, X.-Y.; Karunadasa, H. I., *J. Phys. Chem. Lett.* **2016,** *7*, 2258-2263.
36. McCall, K. M.; Stoumpos, C. C.; Kostina, S. S.; Kanatzidis, M. G.; Wessels, B. W., *Chem. Mater.* **2017,** *29*, 4129–4145.
37. Li, Y.; Lin, C.; Zheng, G.; Cheng, Z.; You, H.; Wang, W.; Lin, J., *Chem. Mater.* **2006,** *18*, 3463-3469.
38. Dohner, E. R.; Hoke, E. T.; Karunadasa, H. I., *J. Am. Chem. Soc* **2014,** *136*, 1718-1721.
39. Dohner, E. R.; Jaffe, A.; Bradshaw, L. R.; Karunadasa, H. I., *J. Am. Chem. Soc* **2014,** *136*, 13154-13157.
40. Yangui, A.; Garrot, D.; Lauret, J.-S.; Lusson, A.; Bouchez, G.; Deleporte, E.; Pillet, S.; Bendeif, E.-E.; Castro, M.; Triki, S., *J. Phys. Chem. C.* **2015,** *119*, 23638-23647.
41. Thirumal, K.; Chong, W. K.; Xie, W.; Ganguly, R.; Muduli, S. K.; Sherburne, M.; Asta, M.; Mhaisalkar, S.; Sum, T. C.; Soo, H. S.; Mathews, N., *Chem. Mater.* **2017,** *29*, 3947–3953.
42. Kortüm, G.; Braun, W.; Herzog, G., *Angew. Chem. Int. Ed.* **1963,** *2*, 333-341.
43. Hohenberg, P.; Kohn, W., *Phys. Rev.* **1964,** *136*, B864.
44. Kohn, W.; Sham, L. J., *Phys. Rev.* **1965,** *140*, A1133.
45. Soler, J. M.; Artacho, E.; Gale, J. D.; García, A.; Junquera, J.; Ordejón, P.; Sánchez-Portal, D., *J. Phys. Condens. Matter* **2002,** *14*, 2745.
46. Cooper, V. R., *Phys. Rev. B* **2010,** *81*, 161104.
47. Yuk, S. F.; Pitike, K. C.; Nakhmanson, S. M.; Eisenbach, M.; Li, Y. W.; Cooper, V. R., *Sci. Rep.* **2017,** *7*.
48. Troullier, N.; Martins, J. L., *Phys. Rev. B* **1991,** *43*, 1993.
49. Zhang, Y.; Yang, W., *Phys. Rev. Lett.* **1998,** *80*, 890.
50. Even, J.; Pedesseau, L.; Kepenekian, M., *Phys. Chem. Chem. Phys.* **2014,** *16*, 25182-25190.
51. Sapori, D.; Kepenekian, M.; Pedesseau, L.; Katan, C.; Even, J., *Nanoscale* **2016,** *8*, 6369-6378.
52. Stoumpos, C. C.; Mao, L.; Malliakas, C. D.; Kanatzidis, M. G., *Inorg. Chem.* **2016,** *56*, 56-73.
53. Geselle, M.; Fuess, H., *Z. KRIST. -NEW CRYST. ST.* **1997,** *212*, 241-242.
54. Im, J.-H.; Chung, J.; Kim, S.-J.; Park, N.-G., *Nanoscale Res. Lett.* **2012,** *7*, 353.
55. Fagnou, K.; Lautens, M., *Angew. Chem. Int. Ed.* **2002,** *41*, 26-47.
56. Alonso, J.; Martinez-Lope, M.; Casais, M.; Fernandez-Diaz, M., *Inorg. Chem.* **2000,** *39*, 917-923.
57. Lufaso, M. W.; Woodward, P. M., *Acta Cryst. B* **2004,** *60*, 10-20.

58. Katan, C.; Pedesseau, L.; Kepenekian, M.; Rolland, A.; Even, J., *J. Mater. Chem. A* **2015,** *3*, 9232-9240.
59. Even, J.; Pedesseau, L.; Dupertuis, M.-A.; Jancu, J.-M.; Katan, C., *Phys. Rev. B* **2012,** *86*, 205301.
60. Bokdam, M.; Sander, T.; Stroppa, A.; Picozzi, S.; Sarma, D.; Franchini, C.; Kresse, G., *Sci. Rep.* **2016,** *6*.
61. Amat, A.; Mosconi, E.; Ronca, E.; Quarti, C.; Umari, P.; Nazeeruddin, M. K.; Grätzel, M.; De Angelis, F., *Nano Lett.* **2014,** *14*, 3608-3616.
62. Knutson, J. L.; Martin, J. D.; Mitzi, D. B., *Inorg. Chem.* **2005,** *44*, 4699-4705.
63. Filip, M.; Eperon, G.; Snaith, H.; Giustino, F., *Nature Commun.* **2013,** *5*, 5757-5757.
64. Smith, M. D.; Pedesseau, L.; Kepenekian, M.; Smith, I. C.; Katan, C.; Even, J.; Karunadasa, H. I., *Chem. Sci.* **2017,** *8*, 1960-1968.
65. Kieslich, G.; Sun, S.; Cheetham, A. K., *Chem. Sci.* **2014,** *5*, 4712-4715.

TOC Graphic